ARTICLE   OPEN

Polaron freezing and the quantum liquid-crystal phase in the ferromagnetic metallic $La_{0.67}Ca_{0.33}MnO_3$

Nikolaos Panopoulos[1], Michael Pissas[1], Hae Jin Kim[2], Jin-Gyu Kim[2], Seung Jo Yoo[2], Jamal Hassan[3], Yasser AlWahedi[4], Saeed Alhassan[4], Michael Fardis[1], Nikos Boukos[1] and Georgios Papavassiliou[1]

The remarkable electronic properties of colossal magnetoresistive manganites are widely believed to be caused by the competition between a ferromagnetic metallic state and an antiferromagnetic insulating state with complex spin, charge, and orbital ordering. However, the physics underlying their magnetotransport properties is still not clear, especially the role of correlated Jahn–Teller polarons, which depending on temperature and doping, might form a liquid, glass or stripe polaron state. This question touches one of the most fundamental problems in the physics of doped Mott insulators, i.e. understanding the mechanism that chemical doping makes an insulator becoming superconductive as in the case of cuprates, or exhibiting the colossal magnetoresistance effect, as in the case of manganites. Here, by using ^{139}La NMR and high resolution transmission electron microscopy in the temperature range 3.2–1000 K, we have monitored the formation and evolution of CE-type polarons in optimally doped $La_{0.67}Ca_{0.33}MnO_3$. While NMR experiments show that correlated polarons dominate electron spin dynamics in the ferromagnetic phase, at very low temperatures they appear to form a quantum liquid-crystal like ferromagnetic phase, embedded into a ferromagnetic matrix with 3D polaron correlations. This is evidence that similarly to high T_c cuprates, quantum soft phases underlie the exotic physical properties of colossal magnetoresistive manganites.

INTRODUCTION

Polarons, moving electrons dressed in a cloth of lattice distortions, are key ingredient in the fascinating physics of transition metal oxides, such as high T_c superconducting cuprates, nickelates, and colossal magnetoresistive (CMR) manganites.[1–9] The concept of polarons was first introduced by Landau in 1933.[10] If an electron is placed into the conduction band of an ionic crystal, the electron is trapped by digging its own hole due to the strong coulombic interaction of the electron with its surrounding positive ions. The electron together with the lattice distortions induced by itself is called polaron (lattice polaron). In addition to this static effect, moving electrons induce dynamic lattice distortions; they are accompanied by lattice vibrations, i.e. phonons. Considering that Cu^{2+} and Mn^{3+} are among the strongest Jahn–Teller (JT) ions, a great effort has been devoted to understand the role of JT polarons in the superconducting pairing of high T_c cuprates,[1–4] and its normal state analog, the CMR effect in manganites.[5–9]

Important role in the efforts to understand superconductivity has been played by the discovery of the hole stripe phase in underdoped cuprates.[11,12] When adding holes into the antiferromagnetic (AFM) insulating parent cuprate, the AFM phase breaks into domains, which are separated by hole-rich metallic clumps (stripes) with a rapid change of the phase of the background spins and orbitals at the domain boundary.[11–13] At the same time a weak energy gap emerges at temperatures 2–3 times T_c,[1,14] giving rise to the so called pseudogap phase. A plausible explanation of the hole-striped phase is in terms of inter-site JT bipolarons.[1,15] At

high temperatures bipolarons occupy random positions, which are accompanied by large strain fields, while by decreasing temperature bipolarons are organized into hole-stripes minimizing their strain energy.

However, in the last years there is compelling evidence that hole assembling in the pseudogap phase of cuprate superconductors is organized in an electronic liquid crystal phase (ELC).[16–19] Scanning tunneling microscopy (STM) experiments demonstrated the formation of large electron nematic domains (>40 nm) on the surface of the BSCCO superconductor.[20] Theoretical calculations have shown that the formation of an ELC state is possible in a hole-doped Mott insulator if zero point transverse stripe fluctuations are above a certain threshold. Then, a novel smectic quantum phase is formed with crystalline order in one direction, and liquid-like correlations in the other two directions.[21]

In the case of hole-doped manganites, exemplified by the prototype $La_{1-x}Ca_xMnO_3$ (LCMO) family, charge segregation phenomena might be viewed with a similar rationale.[22] Manganites resemble in many aspects the cuprate compounds, despite the absence of superconductivity. Like cuprates, manganites are JT active, so there is a certain doping regime, where electron–phonon coupling dominates the electronic and structural properties. Furthermore, they acquire high volume density of dynamic and static JT polarons, which give rise to strong correlation effects.[8,23,24] For example, dynamic short-range polaron correlations give rise to a polaron liquid,[6,25] which by lowering temperature freezes into a polaron glass,[5,9] while in

[1]Institute of Nanoscience and Nanotechnology, NCSR, Demokritos, 153 10 Aghia Paraskevi, Athens, Greece; [2]Korea Basic Science Institute, Daejeon 350-333, Republic of Korea; [3]Department of Physics, Khalifa University of Science and Technology, 127788 Abu Dhabi, UAE and [4]Department of Chemical Engineering, Khalifa University of Science and Technology, 127788 Abu Dhabi, UAE
Correspondence: Georgios Papavassiliou (g.papavassiliou@inn.demokritos.gr)

npj

Polaron freezing and the quantum liquid-crystal phase
N Panopoulos et al.

2

other cases static long-range ordering drives them into a polaron solid.[26] Besides, experiments provide evidence about the presence of a pseudogap-like phase, which is interwoven with polaron ordering,[6,27–29] and the appearance of charge and orbital stripes.[25,30,31] This sets into question the assumption that the pseudogap state is a hallmark of high T_c superconductivity state, suggesting that it is probably a more general phenomenon characteristic of hole-doped AFM Mott insulators. Most important, neutron scattering[32] and high resolution TEM[33] experiments indicate the presence of a smectic[32] and nematic[33] liquid crystal state in the charge stripe phase of manganites. It is thus of fundamental importance to examine in more detail the role of polarons in charge segregation effects, especially the relation of polarons with the formation of an ELC state.

Crucial role in these effects is played by the CE type spin, charge, and orbital ordering, exemplified by the half doped $La_{0.5}Ca_{0.5}MnO_3$ (LCMO(0.5)).[34] The low temperature charge and spin structure in this system is dominated by the CE AFM ordering comprised of alternating Mn^{3+} and Mn^{4+} ions in a zig-zag arrangement on the (001) plane, whereas successive planes are AFM ordered. In addition, a minority ferromagnetic (FM) phase has been observed coexisting with the CE AFM phase.[35,36] Most spectacular, Fresnel imaging and electron holography experiments have shown that the FM minority phase comprises of FM metallic and FM charge ordered regions separated by boundaries with antiphase spin orientation.[37] The question thus rises whether "FM charge ordered—FM metallic" phase segregation in AFM background is present at optimal doping $x = 0.33$, as foreseen by theory,[36] and the relation it might have with the CE-type short range correlated polarons (i.e. short zig-zag chains of alternating Mn^{3+} and Mn^{4+} ions) detected in the PM phase.[9] Most important, in view of the common trends, which have been observed in different doped Mott insulators, to examine whether polaron ordering in manganites might lead to a quantum ELC state at low temperatures.

Here, by using ^{139}La NMR and high resolution transmission electron microscopy (HRTEM) in the temperature range 3.2–1000 K, we succeeded to detect the formation of nanoscopic regions with CE-type charge ordering in the PM phase of LCMO (0.33) and to monitor the evolution of their dynamics by cooling. According to the NMR relaxation experiments, the mechanism of the electron spin dynamics remains unchanged in the FM phase, manifesting the dominant role of correlated polarons down to the lowest temperature of NMR measurements. Remarkably, by decreasing temperature the FM phase is shown to split into two components; a slow relaxing one with extremely low magnetic anisotropy resembling an electron spin liquid crystal phase, and a fast relaxing FM component with relatively high magnetic anisotropy, belonging to the initial FM phase with 3D polaronic correlations. At $T = 3.2$ K a weak NMR signal from AFM CE-type ordered regions was detected, which shows that charge ordering survives down to the lowest temperature of NMR measurements. Most notable, the rapid increase of the low magnetic anisotropy NMR signal component is strong indication that the ground state of FM metallic manganites might be a quantum ELC state, as predicted by theory for doped Mott insulators.[21]

RESULTS

The local static and dynamic magnetic and structural properties of the LCMO(0.33) have been investigated by applying ^{139}La NMR in magnetic field 9.4 T, in the temperature range 3.2 K up to 900 K. In the presence of an external magnetic field B, $^{139}La(I = 7/2)$ nuclei experience the Zeeman interaction, which splits the nuclear energy levels into $2I + 1$ equidistant energy levels, with energies $E_m = m\gamma\hbar B$. In addition, the ^{139}La nucleus is coupled to the local electric field gradient (EFG) tensor, through its electric quadrupolar moment Q. In the presence of both the Zeeman and Quadrupolar

interactions the frequency of the NMR spectrum corresponding to transitions between levels m and m − 1 is given by, $\omega_m = \gamma B + \frac{3}{2}\frac{e^2 qQ}{4\hbar I(2I-1)}(3\cos^2\theta - 1 - \eta\sin^2\theta\cos^2\phi)(2m-1)$, where e is the charge of the electron, eq is equal to V_{zz}, η is the asymmetry parameter of the EFG tensor $\eta = \frac{|V_{yy} - V_{xx}|}{V_{zz}}$, and θ, ϕ are the angles between the principal axis of the EFG tensor and the magnetic field. According to this equation, the transition between the $m = +1/2$ and $m = -1/2$ levels (the so called central transition) is unaffected by the electric quadrupole interaction to first order, while the distance in frequency of all other transitions (satellites) from the central transition, depends solely on the quadrupolar interaction. In case of a powder sample, as in our case, the crystal axes, and hence the EFG, are distributed at random angles with respect to the applied magnetic field. The angular average of the satellite patterns gives rise to a characteristic frequency distribution. The width of the sattelite frequency distribution (SFD) is proportional to the EFG (and consequently to the lattice distortions) and independent of the magnetic field. It is furthermore noticed that for $T < T_c$ the magnetic field B at the site of the La nuclei is equal to the sum of the applied external field B and the transferred hyperfine field $B_{hf} = (1/\gamma\hbar)A\langle S\rangle$, where A is the hyperfine coupling constant and $\langle S\rangle$ the average electronic spin of the eight nearest Mn neighbors.[38,39]

Figure 1a demonstrates ^{139}La NMR spectra of the LCMO(0.33) system in the temperature range 3.2–900 K. LCMO(0.33) undergoes two major phase transitions: a structural one from the high temperature $R\overline{3}c$ rhombohedral phase to the low temperature orthorombic $Pnma$ phase at $T_{RO} \approx 710$ K,[39,40] and a paramagnetic to FM (PM–FM) one at $T_c = 267$ K, as shown in Figures S3.1, S3.2 and S5.1 of the Supplementary Information. The critical temperature of the PM–FM phase transition T_c, defined as the inflection point of the frequency vs. T plot, in the magnetic field of 9.4 T is found to be $T_c \approx 300$ K (right bottom inset), sufficiently higher than in zero external magnetic field. At high temperatures spectra show the characteristic NMR powder pattern consisting of a narrow central line and the broad SFD. However, by approaching T_c from above, the narrow central line starts to broaden and for $T \leq 320$ K becomes indistinguishable from the SFD. The inset at the top left side of Fig. 1a shows the SFD as a function of temperature. By decreasing temperature, at $T \approx 710$ K, an abrupt increase of the SFD width is observed, which marks the transition from the $R\overline{3}c$ to the $Pnma$ crystal structure and the onset of strong incoherent JT displacements.[39,40] Neutron scattering experiments indicate that the appearance of the JT distortions is related with the formation of uncorrelated dynamic JT polarons right below T_{RO}, which by further decreasing temperature freeze into a CE-type polaron glassy state with correlation length of ≈ 1 nm.[9] Most notable, for $T < 100$ K spectra start to broaden and shift to higher frequency, which might indicate the onset of an until now unnoticed novel FM phase. Furthermore, at $T = 3.2$ K, in addition to the FM ^{139}La NMR signal at ≈ 79 MHz, a weak signal is observed at frequency ≈ 58 MHz, which corresponds to the CE-type AFM spin arrangement, as clearly seen in Fig. 1b,c. For reasons of comparison the CE-type AFM NMR signal at $T = 3.2$ K of LCMO(0.50) and LCMO(0.41) are shown in Fig. 1d,e. This result corroborates with theoretical predictions, which show that the FM metallic state of the LCMO family, might be more complicated than initially thought, with the ground state at certain doping concentrations consisting of a CE-type matrix with FM metallic stripes.[36]

To get insight into the evolution of the magnetic interactions in the static polaron regime of the PM phase the inverse NMR central line width $1/w$, which is proportional to the inverse of the magnetic susceptibility χ^{-1},[41] is plotted as a function of temperature in Fig. 2. For reasons of comparison $1/w$ vs. T curves of LCMO with $x = 0.23$, 0.41, and $La_{0.70}Sr_{0.30}MnO_3$ (LSMO(0.30)), from previous ^{139}La NMR line shape measurements[39] are

Polaron freezing and the quantum liquid-crystal phase
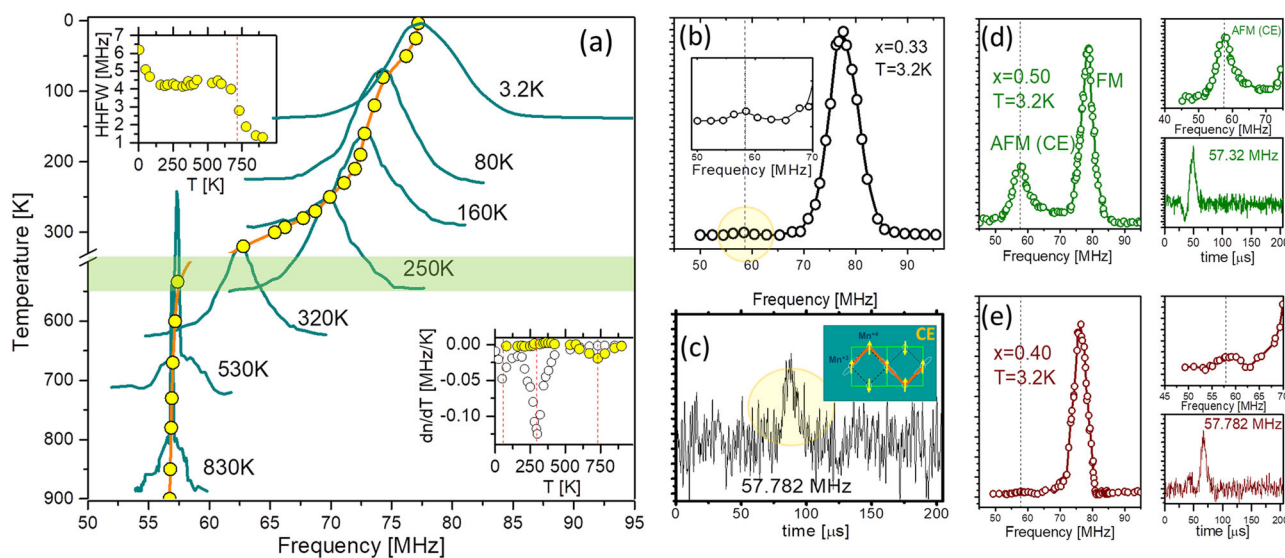N Panopoulos et al.

npj

3

Fig. 1 **a** ^{139}La NMR spectra in magnetic field 9.4 T, in the temperature range 3.2 K up to 900 K. The yellow points show the plot of the NMR frequency as a function of temperature. The upper left inset demonstrates the width of the satellite frequency distribution (SFD) as function of temperature. The bottom right inset shows the derivative of the SFD width (yellow points) and of the NMR signal frequency (white points) as a function of temperature. The structural transition at $T \approx 710$ K and the PM–FM magnetic transition at ≈ 300 K are nicely detected. In addition, a second magnetic phase transition is observed to take place at ≈ 100 K. **b** ^{139}La NMR spectra of LCMO(0.33) at 3.2 K. A weak CE-type AFM signal is observed at frequency 57.782 MHz. **c** The ^{139}La NMR spin-echo signal at 57.782 MHz. **d,e** For reasons of comparison the ^{139}La NMR signal of LCMO(0.50) and LCMO(0.41) are presented. In case of LCMO(0.50) a strong AFM CE-type NMR signal is observed at frequency ≈ 57.6 MHz, together with the FM signal at ≈ 79 MHz[35]
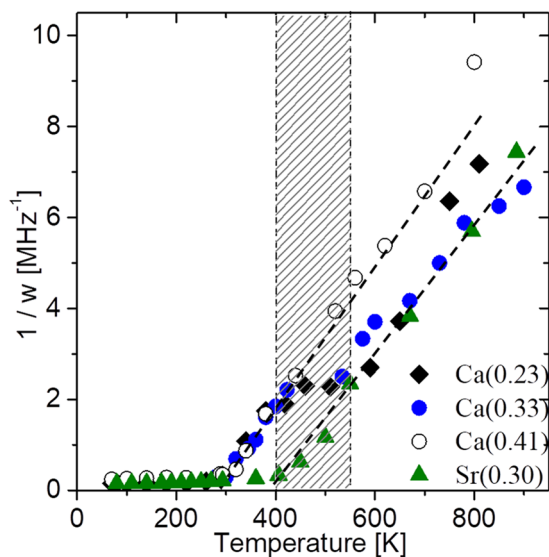

Fig. 2 Formation of static JT polarons affects the inverse ^{139}La NMR linewidth $1/w$, which is proportional to the inverse magnetic susceptibility χ^{-1}.[41] Presented are $1/w$ vs. T curves for LCMO (0.25,0.33,0.41) and LSMO(0.3) in the temperature range 80–900 K and 9.4 T external magnetic field. Strong deviation from the Curie–Weiss law is observed at $T \approx 550$ K for LCMO (0.23, 0.33). The dashed lines are guides to the eye

presented. In case of the LSMO(0.30) system, which remains in the $R\bar{3}c$ crystallographic phase at all temperatures, $1/w$ vs. T follows a linear Curie–Weiss law, crossing the horizontal T axis at $T_c \approx 400$ K. Similarly, LCMO(0.41), which shows only dynamic CE-type polaronic distortions in the PM phase,[9] and no SFD was observed in the relevant ^{139}La NMR spectra, $1/w$ follows the Curie–Weiss law down to $T_c \approx 300$ K. However, in case of LCMO(0.23) and LCMO

(0.33), where JT static polarons have been detected with neutron scattering experiments,[9] strong deviation from the linear Curie–Weiss relation is observed in the temperature range 400–550 K, in agreement with magnetic susceptibility measurements.[40] This deviation signalizes the transition from the dynamic to the static polaron regime.[9,39,40] It is also tempting to consider that for $T > 550$ K electron spin dynamics in both the LCMO (0.23,0.33) systems are dominated by magnetic correlations of the high temperature $R\bar{3}c$ phase, while for $T < 400$ K the formation of the static CE-type polaronic distortions dominates their magnetic properties.

The $Pnma$ to $R\bar{3}c$ phase transition at $T = 710$ K in LCMO(0.33) was identified by applying HRTEM. Since these two phases are very similar, a detailed simulation of their selected area electron diffraction patterns was performed in order to identify zones axes with prominent differences. Using the hexagonal description of the unit cell, two equivalent zone axes are the $[111]_{Pnma}$, which is parallel to $[\bar{1}11]_{R\bar{3}c}$. Figure 3a shows a HRTEM image at room temperature parallel to $[111]_{Pnma}$, while Fig. 3c is the relevant FFT. It should be noted that as an aid to the reader, the usual grey-scale contrast of the HRTEM images in Fig. 3 are converted to a color-scale image, using the temperature color look-up table palette of the Gatan Digital Micrograph software, in order to enhance the contrast details of the HRTEM images (details are presented in Figure S2.6). After heating the same crystal to 800 K the HRTEM image of Fig. 3b was obtained, with the FFT shown in Fig. 3d. The main difference between the two FFTs is that two rows of spots in the $[111]_{Pnma}$ zone axis disappear at 800 K, and the later FFT can only be indexed as the $[\bar{1}11]_{R\bar{3}c}$ zone axis, i.e. the crystal structure at 800 K has changed to the $R\bar{3}c$. HRTEM images in Figures S2.3, S2.4, and S2.5 of the Supplementary Information confirm that for $T < 700$ K the system is in the $Pnma$ phase.

Apart the above crystalline phase transition, another interesting observation was made regarding the $Pnma$ phase at room temperature. Figure 4 presents the HRTEM image parallel to the $[113]_{Pnma}$ zone axis, which provides a clear view of the Mn ions on the $(\bar{2}20)$ planes. Line profile analysis along the $(\bar{1}\bar{2}1)$ planes,
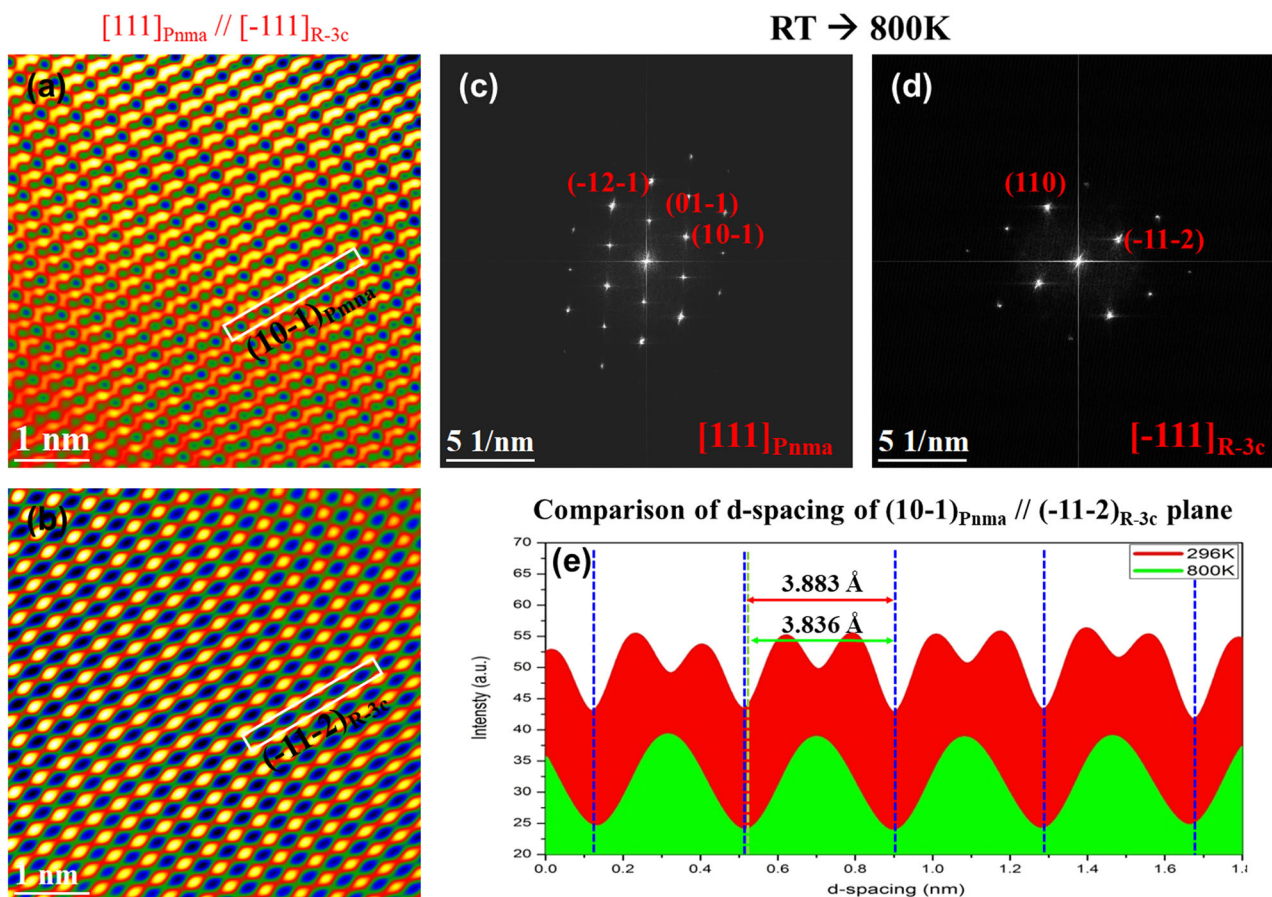
npj

Polaron freezing and the quantum liquid-crystal phase
N Panopoulos et al.

4

Fig. 3 HRTEM detection of the *Pnma* to *R$\bar{3}$c* phase transition of LCMO(0.33) ($T_c \approx 710$ K). **a,b** HRTEM images at $T = 296$ K and $T = 800$ K. **c,d** The relevant fast Fourier transforms. **e** Comparison of the d-spacing along the $(10\bar{1})_{Pnma}//(\bar{1}1\bar{2})_{R\bar{3}c}$ planes. HRTEM measurements in the temperature range 110–1000 K are provided in the Supplementary Information
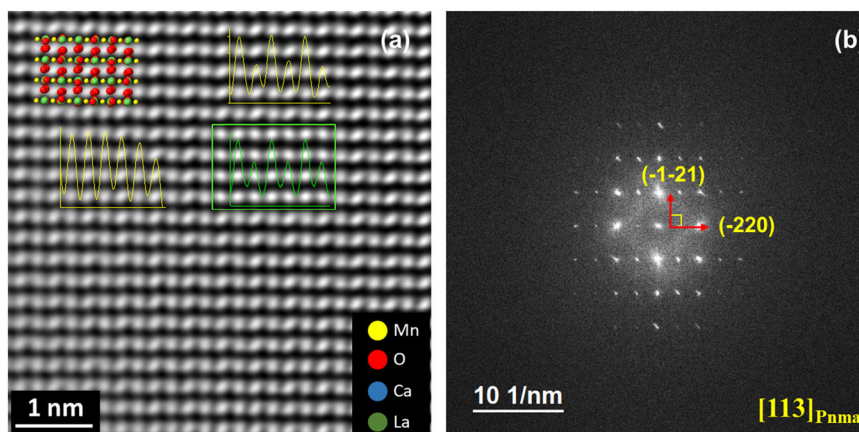
Fig. 4 HRTEM indication of short range charge ordering in the PM phase of LCMO (0.33). **a** HRTEM image parallel to the [113]$_{Pnma}$ zone axis at $T = 296$ K. Intensity profiles along the $(\bar{1}2\bar{1})$ planes are shown in yellow color. The image section in the green rectangle inset is the relevant calculated HRTEM image, as obtained with the MacTempasX software, after performing structural refinement, and including bond-valence sum optimization to consider the presence of Mn^{3+}/Mn^{4+} ions. Comparison of the experimental profiles with the calculated one shows the presence of nanoscopic regions where the two profiles match (upper yellow color profile), indicating the presence of short range charge ordering, as well as regions with no charge ordering (left yellow color profile). **b** The fast Fourier transform of the HRTEM image

shows the presence of nanoscopic regions with size ≈1–2 nm, acquiring alternating profile intensity at the position of successive Mn ions, as shown in the upper yellow intensity profile, while in other regions the profile does not show this type of alteration, as can be seen in the left yellow intensity profile. The green rectangle inset in Fig. 4 is the relevant calculated HRTEM image, which was structurally refined by varying the atomic positions, and by including bond-valence sum optimization to consider the presence of Mn^{3+}/Mn^{4+} ions (Figure S2.7 in the Supplementary Information). Clearly, there exist regions, where the experimental
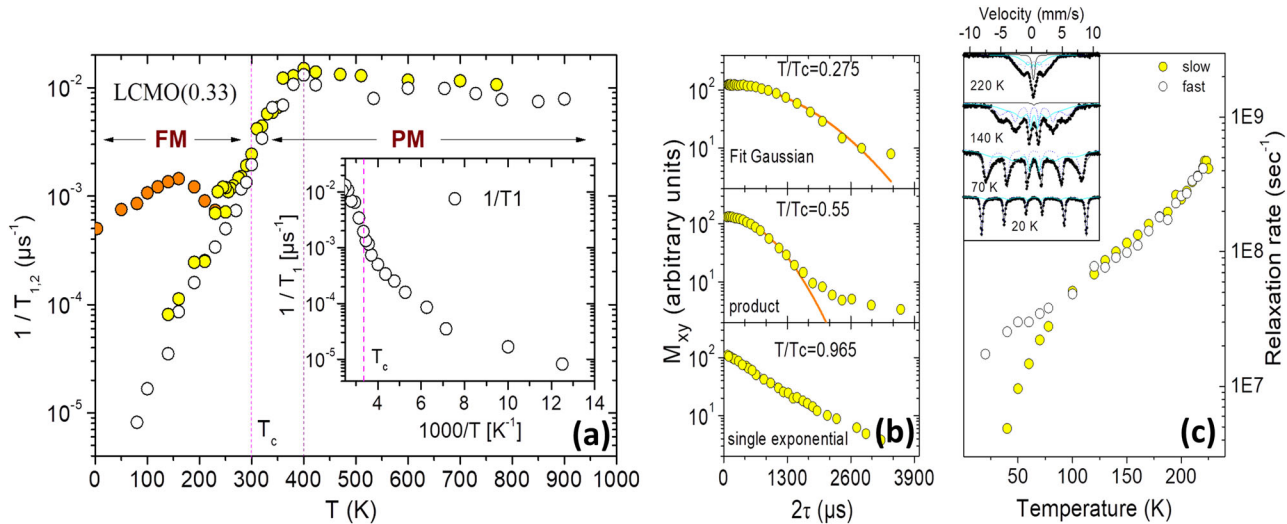
Polaron freezing and the quantum liquid-crystal phase
N Panopoulos et al.

npj

5

Fig. 5 ^{139}La NMR relaxation studies of LCMO(0.33), in external magnetic field of 9.4 T. **a** ^{139}La NMR T_1^{-1} (white points) and $T_2^{-1}/16$ (yellow points) as a function of temperature in the temperature range 3.2–900 K. In the FM phase, T_2^{-1} splits into two components; a fast fluctuating, exponentially decaying one (yellow points) and a slow fluctuating, Gaussian decaying one (orange color points). **b** The decay curves of the ^{139}La NMR transverse magnetization M_{xy} of LCMO(0.33) in external magnetic field of 9.4 T, at three characteristic temperatures. 2τ is the time of refocusing of the nuclear spin echo, as described in the Methods section. **c** ^{57}Fe Moessbauer spectroscopy of $La_{0.67}Ca_{0.32}Fe_{0.01}MnO_3$ as a function of temperature. Measurements confirm the presence of two relaxing components at low temperatures

profiles match with the calculated one, indicating the presence of nanosized charge ordered regions in agreement with previous reports.[34,42]

In order to monitor the evolution of the polaron dynamics across the PM–FM phase transition and in the FM metallic phase, the ^{139}La spin-lattice and spin-spin relaxation (SLR/SSR) rates $T_{1,2}^{-1}$ of the central transition were measured as a function of T by lowering temperature from 900 K down to 3.2 K (Fig. 5a). The pulse sequences and fitting procedures to acquire the T_1 and T_2 relaxation times are described in the Methods section and in ref. [43]. The SLR rate depends on the amplitude and the frequency of the local magnetic field fluctuations $\delta\omega_0$ at the position of the La nuclei, created (i) by the fluctuating part of the transferred hyperfine interaction of the $Mn^{3+,4+}$ ions, and (ii) by the fluctuating part of the dipolar field of the $Mn^{3+,4+}$ ions. According to the literature this can be described as[41,43]

$$\frac{1}{T_1} = \frac{2(\delta\omega_0)^2\tau}{1+(\omega_e\tau)^2} \qquad (1)$$

where $\delta\omega_0 = 2\pi\mu_B A\Sigma\ \delta S_j$, δS_j is the amplitude of the electron spin fluctuation, A is the hyperfine coupling constant, μ_B is the Bohr magneton, ω_e is the electron Larmor frequency, and the correlation time $\tau = \tau_0 \exp(E_a/k_BT)$, which describes polaron hopping through an energy barrier E_a.

Besides, in case of the ^{139}La nuclear sites with $I = 7/2$ the T_1 contribution to the SSR rate is given by $T_2^{-1} = (I + 1/2)^2 T_1^{-1} = 16T_1^{-1}$.[43]

According to Fig. 5a, by lowering temperature both $T_{1,2}^{-1}$ increase gradually until they reach a maximum value $T_{1,max}^{-1} = T_{2,max}^{-1}/16 \approx 10^{-2}\ \mu s^{-1}$ at 400 K, which corresponds to $\omega_e\tau \approx 1$. By further decreasing temperature both SLR and SSR rates decrease abruptly, entering into the slow fluctuating regime, where $\omega_e\tau \geq 1$. No sign of a ferromagnetic critical divergence of the relaxation rates is observed at $T_c = 300$ K, in agreement with previous measurements,[43] which is expected for a soft ferromagnet like LCMO(0.33) in an external magnetic field of 9.4 T. Notably, according to Savosta et al.[44] in the slow fluctuating regime the activation energy E_a of hopping electrons, acquires a

quadratic dependence on temperature, $E_a \propto T^2$, which is attributed to a polaron hopping mechanism for T_1.[44] Comparing the relaxation rates below and above the PM–FM transition, it is evident that for $T < 400$ K the same relaxation mechanism governs electron-spin dynamics in both phases. Remarkably, for $T < 250$ K a second slow relaxing component appears in the SSR rate; This is clearly seen in Fig. 5b which demonstrates the nuclear spin-echo decay curves at three different temperatures in the FMM phase. Right below T_c the spin-echo decays follow a single exponential law and SSR is controlled solely by the SLR contribution, which implies that polaron hopping dominates electron spin dynamics. However, for $T < 120$ K nuclear magnetization is shown to decay with a Gaussian function, which indicates the presence of slow quasistatic electron spin arrangements, resembling the ^{63}Cu nuclear quadrupole resonance (NQR) and NMR spin echo decay of slowly fluctuating stripes in superconducting cuprates.[45,46] In the temperature range 120 K $\leq T \leq$ 250 K both the single exponential and Gaussian T_{2R}^{-1} and T_{2G}^{-1} relaxation mechanisms are present. Remarkably, no change in the SLR rate by cooling is observed, which means that both fast and slow relaxing components are related to the polaron spin dynamics mechanism. The appearance of two phase components with slow and fast dynamics is further confirmed with ^{57}Fe Moessbauer spectroscopy performed on $La_{0.67}Ca_{0.33}Mn_{0.99}Fe_{0.01}O_3$, as presented in Fig. 5c. This system exhibits a PM–FM phase transition at $T_c = 228$ K, which is sufficiently lower than that of the undoped system.[47] Moessbauer spectroscopy, in the ferromagnetic state, measures the hyperfine field B_{hf} via the line splitting at the iron sites. For a typical isotropic ferromagnet, such as α-Fe, Moessbauer spectra (MS) below the critical temperature consist of a sextet with narrow Lorentzian lines, while in the PM phase spectra consist of a single narrow absorption line, which reflects the quadrupolar interactions and the electronic environment via the quadrupolar split and the isomeric shift.[47] The inset in Fig. 5c presents selected MS in the temperature range 20–200 K. At 20 K the spectrum shows two signal components with the characteristic FM sextet, while at higher temperatures they both display an asymmetric line broadening, with dominant the two central lines of the magnetic
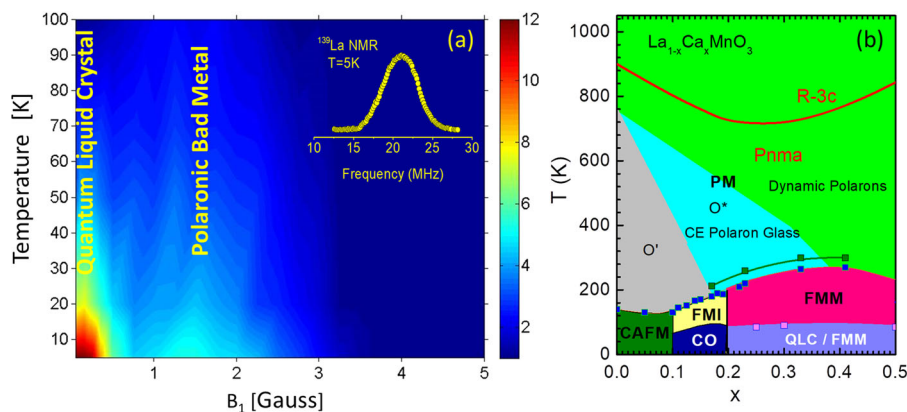
npj

Polaron freezing and the quantum liquid-crystal phase
N Panopoulos et al.

6

Fig. 6 a 2D contour plot of the ^{139}La NMR signal intensity in zero external magnetic field as a function of the rf field B_1 at various temperatures. Measurements were performed at the maximum intensity of the ^{139}La NMR signal at frequency $\approx$21 MHz, as shown in the inset. By lowering temperature a signal component grows for $T < 100$ K, which is excited at extremely low B_1 values. This signal component corresponds to a quantum spin liquid crystal phase, as explained in the text. **b** The temperature vs. Ca doping $T - x$ phase diagram of the La$_{1-x}$Ca$_x$MnO$_3$. A low temperature region of a mixed quantum liquid crystal/FM metallic phase is observed in the doping range $0.2 \leq x \leq 0.5$

sextet. Close to T_c the two central lines appear to collapse partially into a broad single line. This behavior can be excellently fitted with the relaxation model developed by van der Woude and Dekker,[48] unveiling the presence of two different relaxation mechanisms. Specifically, the main plot in Fig. 5c shows the evolution of the relaxation rates of the two Moessbauer signal components with the temperature. While at elevated temperatures a single relaxation rate is observed, at $\approx$100 K the two signals decompose into a fast and slow relaxing components, in similarity with the ^{139}La NMR SSR rate measurements.

The detection of two FM phase components with different spin dynamics corroborates with previous results showing the formation of two FM phase components at low temperatures with different magnetic anisotropy.[49] In order to correlate the two differently relaxing FM components with possible differences in the magnetic anisotropy, the NMR radiofrequency (rf) enhancement technique was implemented. In FM materials, very strong NMR signals are produced at extremely low rf irradiation fields B_1, due to the coupling of the rf field with the magnetic moments of the unpaired electrons.[50] In this way B_1 is strongly enhanced by the rf enhancement factor $n = B_{hf}/(1 + N\chi)B_A$, where N is the demagnetizing factor, χ the magnetic susceptibility, and B_A the magnetic anisotropy field. Correspondingly, the NMR signal is amplified by the oscillating electron moments, thus giving rise to the strong NMR signals that characterize FM materials. Experimentally, the rf enhancement factor is obtained by recording the ^{139}La NMR signal intensity I as a function of B_1 at the peak of the NMR spectra.[50] Since application of an external magnetic field pins electron spins, rf enhancement experiments are performed in zero external magnetic field. The inset in Fig. 6a presents the zero field ^{139}La NMR spectrum of LCMO(0.33) at 5 K. The signal consists of a single broad Gaussian centered at $\approx$21 MHz. The relevant main plot shows the 2D contour plot of the signal intensity vs. B_1 and T. At very low temperatures two signal components are observed at $B_1 \approx 0.1$ and 1.5 G, unveiling the presence of two FM configurations with different magnetic anisotropy. The two signal components correlate excellently with the NMR relaxation and Mossbauer data. It is worth to notice that the signal component with maximum at $B_1 \approx 0.1$, corresponds to FM ordered electron spins responding almost freely to the external rf field, i.e. they possess liquid-like electron spin correlations. By raising temperature this signal decreases in intensity and is not observed for $T > 100$ K (inset in Figure S6.1a), most probably due to the extremely short T_2 value. Furthermore, by increasing the Ca doping the

liquid-like signal component exists even in the AFM LCMO(0.55) system, as presented in Figure S6.1b. At this doping, neutron scattering experiments show only CE-type AFM long-range order (ref. [12] in Supplementary Information). This is evidence that for $x = 0.55$ the detected liquid-like ^{139}La NMR signal is produced in nanoscopic FM regions dispersed in the AFM phase, which are not detectable in neutron scattering experiments. In view of this fact, the observation of the weak CE-type AFM ^{139}La NMR signal in the $x = 0.33$ system indicates that the free responding FM signal is produced in liquid-like FM nanodomains in a background, where AFM CE-type correlations are important. Notably, the planar zig-zag propagation of the CE-type ordering in the (001) plane, make reasonable to consider that the spin-liquid FM nanodomains are ordered into either in-plane nematic threads or smectic (i.e. planar liquid) nanodomains.

DISCUSSION
A plausible scenario explaining these results is as follows: static CE-type polarons are formed in the *Pnma* phase of the LCMO(0.33) system for $T < 550$ K. In the high temperature rhombohedral $R\bar{3}c$ phase JT distortions are forbidden by symmetry, while right below the T_{RO} transition temperature, dynamic JT polarons were detected with the help of neutron scattering experiments.[9] Interestingly, the HRTEM results at room temperature in Fig. 4 indicates the formation of nanoscopic charge ordered regions, with size $\approx$1–2 nm. It is noticed that the CE phase consists of diagonal stripes of alternating zig-zag Mn^{3+} and Mn^{4+} charges (as well as $d(3x^2 - r^2)$ and $d(3y^2 - r^2)$) on the (001) plane, which from the TEM point of view would give rise to an alternating line profile intensity at the position of the Mn ions on successive ($\bar{2}20$) planes. This is similar to the line profile intensity of the calculated HRTEM images in Fig. 4a and S2.7. At this point it should be mentioned that since HRTEM images are phase contrast sensitive, further work is needed to confirm this result. The formation of CE-type polarons corroborates also with the electrical resistivity measurements in zero external magnetic field presented in Figure S4.1 of the Supplementary Information. Specifically, for $T < 300$ K, an anomalous increase of the electrical resistance is observed, which is in agreement with the presence of short-range-ordered polarons, while for $T < T_c \approx 265$ K, the resistivity decreases initially abruptly, and subsequently gradually following a non-metallic temperature dependence. The abrupt decrease of the resistivity right below T_c is evidence that part of the static polaron regions

Polaron freezing and the quantum liquid-crystal phase
N Panopoulos et al.

7

melt into a polaron bad metal. Another interesting result is that the appearance of static polarons in the PM phase has strong impact on the magnetic susceptibility, as seen in the inverse ^{139}La line width $1/w$ vs. T curve, which is observed to deviate strongly from the Curie–Weiss law for $T < 550$ K. Most notably, the ^{139}La NMR SLR data in Fig. 5a show that polaron dynamics follow the same law in both the PM and FMM phases, suggesting that spatially extended polaron correlations survive down to the lowest measured temperature. A similar temperature dependence was observed in the ^{139}La NMR SLR rate of $La_{1-x}Na_xMnO_3$, which was acquired in zero external magnetic field for $T < T_c$.[44] For $T < 200$ K the ^{139}La NMR spin echo decay envelope becomes gradually Gaussian, as observed in Fig. 4b, which is evidence that polaron dynamics freeze down. A slow relaxing FM phase component is detected at low temperatures with novel features: (i) it has extremely low magnetic anisotropy, as shown by the ^{139}La NMR rf enhancement experiments, and (ii) it shows enhanced spin polarization in an external magnetic field, as implied by the ^{139}La NMR signal frequency shift in Fig. 1a. At the same time a weak AFM CE-type ^{139}La NMR signal has been observed at 3.2 K, which is strong indication that there exist nanoscopic regions, where the CE-type zig-zag spin and charge ordering survives down to the lowest measured temperature. A reasonable assumption to explain the extremely low magnetic field anisotropy in conjunction with CE-type ordering is that at low temperatures, in the FM metallic phase an electron spin liquid crystal phase component appears, which is comprised of uncorrelated CE-type zig-zag FM polaron chains. Notably, the strong enhancement of the intensity of the NMR signal from the low magnetic anisotropy regions by cooling down to the lowest measured temperature of 5 K, as presented in the inset of Figure S7.1a, is indication that the electron spin liquid crystal phase might be the ground state of this system. The above scenario is comprehended into the phase diagram presented in Fig. 6b, where a region with mixed FM metallic spin crystalline/FM quantum spin liquid crystal phase is observed to exist in the doping region $0.2 \leq x \leq 0.5$.

In summary, by using ^{139}La NMR and HRTEM in the temperature range 3.2–900 K, we succeeded to elucidate important aspects on the role of polarons in the intriguing physical properties of optimally doped FM LCMO(0.33). We present strong indications that for $T < 550$ K, the PM phase is organized into quasistatic CE-type correlated polarons, while for $T < T_c$ these regions transform into a bad polaronic metal, possibly on a dynamic CE-type background. This is reminiscence of the STM and ARPES study of $La_{2-2x}Sr_{1+2x}Mn_2O_7$, which uncover this system as a pseudogaped bad polaronic metal.[6] Most important, suppressing thermal fluctuations by decreasing temperature, polarons are shown to organize into a quantum spin liquid crystal phase, presumably of uncorrelated CE-type polaron chains. This is important information in the emerging field of quantum liquid crystal systems.

METHODS

$La_{0.67}Ca_{0.33}MnO_3$ powder sample was prepared by thoroughly mixing high-purity stoichiometric amounts of $CaCO_3$, La_2O_3, and MnO_2. The mixed powder reacted in air up to 1400 °C for several days with intermediate grinding. The sample was then slowly cooled to 25 °C. In order to secure stoichiometry of the sample, additional annealing in He atmosphere was applied. More specifically, in the final preparation step the sample was heated under He flow up to 1100 °C for 48 h followed by rapid cooling to room temperature.

Powder X-ray diffraction (XRD) patterns were acquired at room temperature using a Siemens D500 diffractometer, with Cu K radiation ($\lambda = 1.5418$ Å). XRD patterns were recorded in 2θ ranging from 10° to 120°, at a scanning rate of 0.03°/min. The crystal structure and the exact structural parameters were determined with Rietveld refinement. Simulated XRD patterns were produced by the Fullprof software package (Figure S1.1 in the Supplementary Information).

Samples for electron microscopy were prepared by suspending the LCMO powder in ethanol, followed by air evaporation of a droplet on an ultra thin carbon-supported Cu grid (TED PELLA, Inc.). In-situ TEM investigation of LCMO nano-powders was carried out using the high voltage electron microscope (JEM-ARM1300S, 1250 kV) installed at Korea Basic Science Institute in the temperature range from 100 to 1000 K. The LCMO nano-powders in HVEM were heated/cooled at a rate of 10 K/min and a holding time of 30 min at each temperature. The structure modeling of two phases LCMO crystals was performed according to previous result[40] and the drawing of atomic structure was performed using program VESTA. The quality of all high-resolution electron microscopy (HREM) images was enhanced by using bandpass and mask filtering method with fast Fourier transform (FFT) data of HREM images. Calculated HRTEM images were obtained with the help of the MacTempasX software, Total Resolution LLC. Structural refinement was performed by varying the atomic positions, including bond-valence sum optimization to unveil the Mn^{3+}, Mn^{4+} ordering. The simulated electron diffraction pattern images were obtained with the SingleCrystal software (CrystalMaker Software Ltd.).

^{139}La NMR experiments were performed on a home-built broadband spectrometer operating in the frequency range 5–800 MHz, in 9.4 T and zero external magnetic field. Because the NMR spectra are extremely broad, the $90° - \tau - 180°$ spin-echo point by point method was employed, which is based on recording the spin echo signal, while sweeping the spectrometer frequency. An Oxford 1200CF continuous flow cryostat was employed for measurements in the temperature range 3.2–350 K and an Oxford HT1000V furnace for measurements in the range 300–900 K. In case of the NMR measurements in the 9.4 T external magnetic field, pulse widths were set to 7 and 14 µsec, respectively. In case of the NMR measurements in zero external magnetic field the pulse widths were set at 0.6 and 1.2 µsec and very-low rf power level (B_1 in the range 0.05–5 G) was applied, due to the very strong rf-enhancement factor which characterizes magnetic materials in the absence of a strong external magnetic field. ^{139}La NMR spin-lattice T_1 measurements were performed by using a $90° - t - 90° - \tau - 180°$ pulse sequence, comprised of a saturation recovery two-pulse sequence, followed by a 180° pulse to record the spin echo signal. ^{139}La NMR spin-spin T_2 measurements were performed by using the conventional $90° - \tau - 180°$ Hahn spin echo pulse sequence.

Absorption MS were collected with a ^{57}Co(Rh) source moving at room temperature, while the absorbers were in a variable temperature cryostat.

DC magnetization measurements, electrical resistance and heat capacity measurements, which are presented in the Supplementary Information, were performed on a Quantum Design, Physical Property Measuring System (PPMS-9T) operating in magnetic fields 0–9 T and in the temperature range 2–350 K. Specifically, for the electrical resistance measurements the van der Pauw four-point technique in the PPMS was applied on pelletized samples (Figures S3.1, S3.2, S4.1, and S5.1 in the Supplementary Information).

Data availability
The authors declare that the data supporting the findings of this study are available within the article and its Supplementary Information files.

AUTHOR CONTRIBUTIONS
G.P., M.P., H.J.K., J.H., and S.A. conceived the project and have written–corrected the manuscript. M.P. has synthesized the sample. N.P., J.H, M.F., and G.P., performed the NMR experiments. N.P. and M.P. performed the Moessbauer measurements. H.J.K., J.G.K., S.J.Y., and N.B., performed the TEM measurements and the relevant data analysis. M.P., Y.A., and S.A. performed sample characterization and data analysis of XRD, magnetic, resistivity, and heat capacity measurements.

ADDITIONAL INFORMATION

npj

Polaron freezing and the quantum liquid-crystal phase
N Panopoulos et al.

8

REFERENCES

1. Mueller, K. A. *Handbook of High Temperature Superconductivity. Theory and Experiment*. (Springer Verlag, Berlin, 2007).
2. Madan, I. et al. Evidence for carrier localization in the pseudogap state of cuprate superconductors from coherent quench experiments. *Nat. Commun.* **6**, 6958 (2015).
3. Salje, E. K. H., Alexandrov, A. S. & Liang, W. Y. *Polarons and bipolarons in high-t superconductors and related materials*. (Cambridge Univesity Press, Cambridge, 1995).
4. Mishchenko, A. S. et al. Polaronic metal in lightly doped high-Tc cuprates. *Eur. Phys. Lett.* **95**, 57007 (2011).
5. Weber, F. et al. Signature of checkerboard fluctuations in the phonon spectra of a possible polaronic metal $La_{1.2}Sr_{1.8}Mn_2O_7$. *Nat. Mater.* **8**, 798–802 (2009).
6. Massee, F. et al. Bilayer manganites reveal polarons in the midst of a metallic breakdown. *Nat. Phys.* **7**, 978–982 (2011).
7. Li, J. et al. Dichotomy in ultrafast atomic dynamics as direct evidence of polaron formation in manganites. *npj Quantum Mater.* **1**, 16026 (2016).
8. Alexandrov, A. S. & Bratkovsky, A. M. Carrier density collapse and colossal magnetoresistance in doped manganites. *Phys. Rev. Lett.* **82**, 141–144 (1999).
9. Lynn, J. W. et al. Order and dynamics of intrinsic nanoscale inhomogeneities in manganites. *Phys. Rev. B* **76**, 014437 (2007).
10. Landau, L. D. On the motion of electrons in a crystal lattice. *Phys. Z. Sowjet.* **3**, 664–665 (1933).
11. Tranquada, J. M. et al. Evidence for stripe correlations of spins and holes in copper oxide superconductors. *Nature* **375**, 561–563 (1995).
12. Tranquada, J. M. et al. Coexistence and competition between superconductivity and charge-stripe order in $La_{1.6-x}Nd_{0.4}Sr_xCuO_4$. *Phys. Rev. Lett.* **78**, 338–341 (1997).
13. Emery, V. J., Kivelson, S. A. & Tranquada, J. M. Stripe phases in high-temperature superconductors. *Proc. Natl Acad. Sci. USA* **96**, 8814–8817 (1999).
14. Daou, R. et al. Broken rotational symmetry in the pseudogap phase of a high-Tc superconductor. *Nature* **463**, 519–522 (2010).
15. Mihailovic, D. & Kabanov, V. V. Finite wave vector Jahn-Teller pairing and superconductivity in the cuprates. *Phys. Rev. B* **63**, 054505 (2001).
16. Pelc, D. et al. Unconventional charge order in a co-doped high-T_c superconductor. *Nat. Commun.* **7**, 12775 (2016).
17. Phillabaum, B., Carlson, E. W. & Dahmen, K. A. Spatial complexity due to bulk electronic nematicity in a superconducting underdoped cuprate. *Nat. Commun.* **3**, 915 (2012).
18. Ando, Y., Segawa, K., Komiya, S. & Lavrov, A. Electrical resistivity anisotropy from self-organized one dimensionality in high-temperature superconductors. *Phys. Rev. Lett.* **88**, 137005 (2002).
19. Hinkov, V. et al. Electronic liquid crystal state in the high-temperature superconductor $YBa_2Cu_3O_{6.45}$. *Science* **319**, 597–600 (2008).
20. Lawler, M. J. et al. Intra-unit-cell electronic nematicity of the high-Tc copper oxide pseudogap states. *Nature* **466**, 347–351 (2010).
21. Kivelson, S. A., Fradkin, E. & Emery, V. J. Electronic liquid-crystal phases of a doped Mott insulator. *Nature* **393**, 550–553 (1998).
22. Dagotto, E. Open questions in CMR manganites, relevance of clustered states and analogies with other compounds including the cuprates. *New. J. Phys.* **7**, 67 (2005).
23. Zhao, G. M. Polarons in colossal magnetoresistive and high-temperature superconducting materials. Polarons in advanced materials. *Springer Ser. Mater. Sci.* **103**, 569–597 (2007).
24. Zhao, G. M., Conder, K., Keller, K. & Mueller, K. A. Giant oxygen isotope shift in the magnetoresistive perovskite $La_{1-x}Ca_xMnO_{3+y}$. *Nature* **381**, 676–678 (1996).
25. Campbell, B. J. et al. Structure of nanoscale polaron correlations in $La_{1.2}Sr_{1.8}Mn_2O_7$. *Phys. Rev. B* **65**, 014427 (2001).
26. Jooss, Ch et al. Polaron melting and ordering as key mechanisms for colossal resistance effects in manganites. *Proc. Natl Acad. Sci. USA* **104**, 13597–13602 (2007).
27. Chuang, Y.-D. et al. Fermi surface nesting and nanoscale fluctuating charge/orbital ordering in colossal magnetoresistive oxides. *Science* **292**, 1509–1512 (2001).
28. Mannella, N. et al. Nodal quasiparticle in pseudogapped colossal magnetoresistive manganites. *Nature* **438**, 474–478 (2005).
29. Mannella, N. et al. Polaron coherence condensation as the mechanism for colossal magnetoresistance in layered manganites. *Phys. Rev. B* **76**, 233102 (2007).
30. Loudon, J. C. et al. Weak charge-lattice coupling requires reinterpretation of stripes of charge order in $La_{1-x}Ca_xMnO_3$. *Phys. Rev. Lett.* **94**, 097202 (2005).
31. Maniadis, P., T. Lookman, T. & Bishop, A. R. Elastically driven polaron patterns: stripes and glass phases. *Phys. Rev. B* **84**, 024304 (2011).
32. Ye, F. et al. Electronically smecticlike liquid-crystal phase in a nearly half-doped manganite. *Phys. Rev. B* **72**, 212404 (2005).
33. Tao, J. et al. Direct observation of electronic liquid-crystal phase transitions and their microscopic origin in $La_{1/3}Ca_{2/3}MnO_3$. *Sci. Rep.* **6**, 37624 (2016).
34. Salamon, M. B. & Jaime, M. The physics of manganites: structure and transport. *Rev. Mod. Phys.* **73**, 583–628 (2001).
35. Koumoulis, D. et al. Direct NMR evidence of phase solitons in the spin ground state of overdoped manganites. *Phys. Rev. Lett.* **104**, 077204 (2010).
36. Sen, C., Liang, S. & Dagotto, E. Complex state found in the colossal magnetoresistance regime of models for manganites. *Phys. Rev. B* **85**, 174418 (2012).
37. Loudon, J. C., Mathur, N. D. & Midgley, P. A. Charge-ordered ferromagnetic phase in $La_{0.5}Ca_{0.5}MnO_3$. *Nature* **420**, 797–800 (2002).
38. Papavassiliou, G. et al. Polarons and phase separation in lanthanum-based manganese perovskites: a ^{139}La and ^{55}Mn NMR study. *Phys. Rev. B* **59**, 6390 (1999).
39. Panopoulos, N. et al. Spin order and lattice frustration in optimally doped manganites. A high temperature NMR study. *Phys. Rev. B* **82**, 235102 (2010).
40. Souza, J. A. et al. Polaron liquid-gas crossover at the orthorhombic-rhombohedral transition of manganites. *Phys. Rev. B* **78**, 054411 (2008).
41. Sakaie, K. E. et al. ^{139}La spectrum and spin-lattice relaxation measurements of $La_{2/3}Ca_{1/3}MnO_3$ in the paramagnetic state. *Phys. Rev. B* **59**, 9382 (1999).
42. Zuo, J. M. & Tao, J. Nanometer-sized regions of charge ordering and charge melting in $La_{2/3}Ca_{1/3}MnO_3$ revealed by electron microdiffraction. *Phys. Rev. B* **63**, 060407R (2001).
43. Allodi, G., De Renzi, R. & Guidi, G. ^{139}La NMR in lanthanum manganites: Indication of the presence of magnetic polarons from spectra and nuclear relaxations. *Phys. Rev. B* **57**, 1024–1034 (1998).
44. Savosta, M. M., Borodin, V. A. & Novak, P. Ferromagnetic manganites: Half-metals versus polaronic conductors. *Phys. Rev. B* **59**, 8778–8783 (1999).
45. Hunt, A. W., Singer, P. M., Thurber, K. R. & Imai, T. ^{63}Cu NQR measurement of stripe order parameter in $La_{2-x}Sr_xCuO_4$. *Phys. Rev. Lett.* **82**, 4300–4303 (1999).
46. Itoh, Y., Machi, T. & Yamamoto, A. Ultraslow fluctuations in the pseudogap states of $HgBa_2CaCu_2O_{6+}$. *Phys. Rev. B* **95**, 094501 (2017).
47. Simopoulos, A. et al. Study of Fe-doped $La_{1-x}Ca_xMnO_3$ ($x \approx 1/3$) using Moessbauer spectroscopy and neutron diffraction. *Phys. Rev. B* **59**, 1263–1271 (1999).
48. Van der Woude, F. & Dekker, A. J. The relation between magnetic properties and the shape of Mssbauer spectra. *Phys. Status Solidi* **9**, 775–786 (1965).
49. Belesi, M. et al. NMR as a local probe of magnetic anisotropy: the possibility of orbital ordering and orbital liquid states in colossal magnetoresistance manganites. *Phys. Rev. B* **63**, 180406 (2001).
50. Papavassiliou, G. et al. Low temperature charge and orbital textures in $La_{0.875}Sr_{0.125}MnO_3$. *Phys. Rev. Lett.* **96**, 097201 (2006).